Contract No:

This document was prepared in conjunction with work accomplished under Contract No. 89303321CEM000080 with the U.S. Department of Energy (DOE) Office of Environmental Management (EM).

Disclaimer:

Proceedings of the ASME 2023
Pressure Vessels & Piping Conference
PVP2023
July 16-21, 2023, Atlanta, Georgia, USA

Draft

PVP2023-106161

DATA-DRIVEN STRESS INTENSITY FACTOR SOLUTIONS FOR AXIAL OUTSIDE SURFACE CRACKS IN THIN-WALLED CYLINDERS

Xian-Kui Zhu
Materials Technology
Savannah River National Laboratory
Aiken, SC 29808, USA

Jesse B. Zhu
Microsoft Technology Center
New York, NY 10036, USA

Andrew J. Duncan
Materials Technology
Savannah River National Laboratory
Aiken, SC 29808, USA

ABSTRACT:

In the flaw evaluation, fracture mechanics methods require calculation of stress intensity factor, K, in fitness-for-service (FFS) codes, such as API 579 and ASME BPVC Section XI. For a surface crack in a cylinder, the K calculation becomes to compute the influence coefficients G0 and G1 in the FFS codes. API 579 provides finite element analysis-based tabular data of G0 and G1 for selected cylinder size (t/R_i), crack aspect ratio (a/c), crack depth ratio (a/t), and crack tip locations. Recently, curve-fit solutions of G0 and G1 were obtained for surface cracks at the deepest and surface points. For an arbitrary cylinder, however, three-parameter interpolations are still needed for estimating the G0 and G1.

To simplify the K factor calculation, the present authors (PVP2022-86164) developed a data-driven K factor solution for axial outside surface cracks in thick-walled cylinders ($D/t \leq 20$) based on the API 579 tabular data of G0 and G1 for axial outside semi-elliptical surface cracks at the deepest and surface points using the machine learning technology. This paper further develops a data-driven K factor solution for axial outside surface crack in thin-walled cylinders ($D/t \geq 20$) using the artificial neural network (ANN). The sigmoid activation function is adopted in the optimal learning algorithm for the ANN model to learn from the API 579 tabular data of G0 and G1 and to predict the K solutions at the deepest and surface points for an arbitrary cylinder or crack size. The proposed ANN model contains three input variables, one hidden layer with five neurons, and one output variable. The data-driven solutions of G0 and G1 at the deepest and surface points of the axial outside semi-elliptical surface cracks are validated by the existing closed-form solutions for thin-walled cylinders.

Keywords: stress intensity factor, influence coefficient, curve fit, machine learning, API 579, ASME BPVC

1. INTRODUCTION

Many failures of pressure vessels have been traced to surface cracks. The fracture mechanics assessment of the surface cracks require accurate stress analyses for reliable prediction of crack growth rate and fracture strength. For instance, the fitness-for-service (FFS) codes, such as the American Petroleum Institute (API) 579 [1] and American Society for Mechanical Engineers (ASME) Boiler and Pressure Vessel Code (BPVC) Section XI [2], use the linear elastic or elastic-plastic fracture mechanics methods that require calculation of stress intensity factor, K, for surface cracks. Owing to complexities of surface crack problems, either engineering estimates or approximate analytical methods were utilized to determine the K solutions in the FFS evaluation of pressure vessels or pipelines.

Early engineering estimates of the K factor for surface cracks in pressurized cylinders were made by Underwood [3] and Kobayashi [4, 5]. Numerical calculations of the K factor were performed by Neman and Raju [6, 7] for semi-elliptical surface cracks in a pressurized cylinder using finite element analysis (FEA). Based on the FEA results and the weight function method, Wang and Lamber [8] developed a closed-form solution of the K factor for a thin-walled pipe with a fixed inside radius to wall thickness ratio of $R_i/t=10$. In order to estimate the K factor for any axial surface crack in a thick-walled cylinder subject to an arbitrarily distributed hoop stress, Newman and Raju [6, 7] developed a two-step estimate approach. First, they fit a nonlinear hoop stress on the crack surface using a 3rd-order polynomial function that contains the uniform, linear, quadratic, and cubic terms. Then, the K factor was calculated using the 3D FEA results as the sum of the four specific K factors that were referred to as the boundary correction factors, G0 for the uniform stress, G1 for the linear stress, G2 for the quadratic stress, and G3 for the cubic stress. However, their FEA results were obtained

This work was produced by Battelle Savannah River Alliance, LLC under Contract No. 89303321CEM000080 with the U.S. Department of Energy. Publisher acknowledges the U.S. Government license to provide public access under the DOE Public Access Plan (http://energy.gov/downloads/doe-public-access-plan).

only for two selected cylinders of t/R_i=0.1 and 0.25. As such, Anderson et al. [9] extended the two-step approach to a wide range of cylinder sizes with t/R_i from 0 to 1 and obtained a series of FEA-based tabular data of G0 and G1 for different surface cracks from shallow to deep. These FEA-based tabular data were adopted by API 579 [1].

The tabular data of the K factor in API 579 [1] have been obtained extensive applications in the FFS evaluation of pressure vessels. For convenient use of the API tabular data, Xu et al. [10, 11] employed the nonlinear regression method and obtained a set of curve-fit closed-from solutions of the influence coefficients G0 and G1 for axial inside and outside semi-elliptical surface cracks at the deepest and surface points for the API selected cylinder sizes. For other cylinder sizes, however, three-parameter interpolations are still needed to determine the G0 and G1 values. On the other hand, the machine learning technology becomes matured and has been applied to develop machine learning models of burst strength for pressure vessels [12]. At PVP2022, Zhu et al. [13] developed data-driven stress intensity factor solutions for axial outside surface cracks in thick-walled cylinders that can accurately predict the K solutions for any crack sizes in an arbitrary cylinder of interest.

This paper extends the machine learning method of Zhu et al. [13] to further develop data-driven stress intensity factor solutions for axial outside surface cracks in thin-walled cylinders in reference to the tabular datasets of G0 and G1 given in API 579 [1]. Artificial neural network (ANN) coupling with Sigmoid activation function and optimal learning algorithm is adopted to learn and to predict the K solution as a function of the cylinder size (t/R_i), aspect ratio (a/c), and crack depth (a/t) for an axial outside surface crack at its deepest and surface points. The proposed data-driven solutions of G0 and G1 for axial outside surface cracks are validated by the curve-fit solutions by Xu et al. [9] and the weight function solution by Wang and Lamber [8].

2. TABULAR DATA OF K FACTOR IN API 579

2.1 Engineering estimates of the K factor

Consider an axial outside semi-elliptical surface crack in a pressurized cylinder, as shown in Fig. 1, where R_i is the inside radius, t is the wall thickness, a is the crack depth, and $l = 2c$ is the crack length. In addition, φ is the parametric angle of the semi-elliptical crack, and $\beta = 2\varphi/\pi$. As shown in Fig. 1, Point 1 denotes the deepest point of the crack with $\varphi = \pi/2$ or β=1, and Point 2 denotes the surface point with φ=0 or β=0.

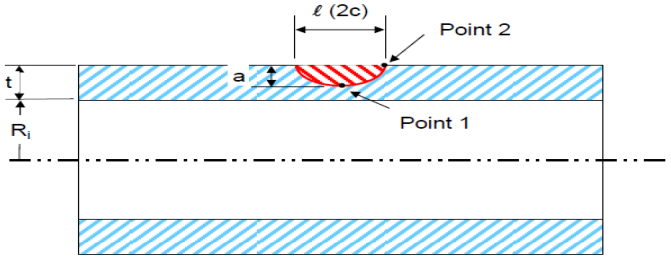

Figure 1. Axial outside semi-elliptical surface crack

As previously introduced, the tabular data of the K factor in API 579 [1] for surface cracks in cylinders were obtained by Anderson et al. [9] from the 3D FEA results. They adopted the two-step engineering estimate approach developed by Newman and Raju [6, 7]. The approach determines the representative stress at the crack location, and then estimates the stress intensity factor. Specifically, the first step is to determine the stress distribution at the crack surface location through the stress analysis of the cracked component under an applied loading in absence of the crack, and the actual stress representation of the nonlinear stress distribution at the crack location is used with five influence coefficients G0, G1, G2, G3 and G4 that are given in API 579 to calculate the K factor for a specific stress on the surface crack in the cylinder, where G0, G1, G2, G3, and G4 are five nondimensional stress intensity factors that correspond to the uniform stress, linear stress, quadratic stress, cubic stress, and quartic stress acting on the crack surface, respectively.

The API 579 tabular data of the K factor make the engineering estimate approach very convenient and efficient to use in estimating stress intensity factor for surface cracks.

2.2 Polynomial representation of stress distribution

For a hollow cylinder subject to combined loading, the hoop stress has a nonlinear distribution through the wall thickness. An actual stress at the crack surface location can be accurately curve-fitted to a 4th-order polynomial function over the wall thickness that is represented in API 579 [1] as:

$$\sigma(x) = \sigma_0 + \sigma_1\left(\frac{x}{t}\right) + \sigma_2\left(\frac{x}{t}\right)^2 + \sigma_3\left(\frac{x}{t}\right)^3 + \sigma_4\left(\frac{x}{t}\right)^4 \quad (1)$$

where $\sigma(x)$ is the representation of actual hoop stress distribution through the wall thickness, x is a local coordinate and measured from the origin on the crack mouth toward the deepest point of the surface crack (see Fig. 1), and σ_j denotes five curve-fit parameters of the polynomial of a general stress distributed on the crack surface. $\sigma(0)=\sigma_0$ is the hoop stress on the outside surface of the cylinder, and $\sigma(t) = \sigma_0 + \sigma_1 + \sigma_2 + \sigma_3 + \sigma_4$ is the hoop stress on the inside surface. Those two hoop stresses are membrane stress and bending stress at the crack location.

For a thick-walled cylinder subject to internal pressure only, the well-known Lamè hoop stress [14] is:

$$\sigma_{\theta\theta} = \frac{PR_i^2}{R_0^2 - R_i^2}\left[1 + \left(\frac{R_0}{r}\right)^2\right] \quad (2)$$

where R_0 is the outside radius of the cylinder, P is the internal pressure, and r is the polar coordinate in a range of $R_i \le r \le R_0$. Using the local x, the hoop stress is approximated by:

$$\sigma_{\theta\theta} = \frac{PR_i^2}{R_0^2 - R_i^2}\left[2 + 2\left(\frac{a}{R_0}\right)^1\left(\frac{x}{a}\right)^1 + 3\left(\frac{a}{R_0}\right)^2\left(\frac{x}{a}\right)^2 + 4\left(\frac{a}{R_0}\right)^3\left(\frac{x}{a}\right)^3 + 5\left(\frac{a}{R_0}\right)^4\left(\frac{x}{a}\right)^4\right] \quad (3)$$

2.3 Stress intensity factor solutions

For the 4th-order polynomial representation of the stress distribution as expressed in Eq. (1), the corresponding stress intensity factor is calculated using the following equation:

$$K_I = \sum_{j=0}^{4} \sigma_j \left(\frac{a}{t}\right)^j G_j \left(\frac{\pi a}{Q}\right)^{\frac{1}{2}} \quad (4)$$

where a is the crack length, c is one half of the crack length, σ_j is the curve-fit coefficient of the stress representation, G_j is the influence coefficients of K_I that correspond to σ_j, K_I is the stress intensity factor for Model-I cracks, and Q is the surface crack shape factor that was defined by Newman and Raju [6, 7] as:

$$Q = \begin{cases} 1 + 1.464\left(\frac{a}{c}\right)^{1.65}, & for\ \frac{a}{c} \le 1 \\ 1 + 1.464\left(\frac{c}{a}\right)^{1.65}, & for\ \frac{a}{c} > 1 \end{cases} \quad (5)$$

For a thick-wall pressure cylinder, using the representative hoop stress in Eq. (3), the K factor in Eq. (4) becomes:

$$K_I = \left(\frac{\pi a}{Q}\right)^{\frac{1}{2}} \frac{PR_i^2}{R_0^2 - R_i^2}\left[2G_0 + 2\left(\frac{a}{R_0}\right)^1 G_1 + 3\left(\frac{a}{R_0}\right)^2 G_2 + 4\left(\frac{a}{R_0}\right)^3 G_3 + 5\left(\frac{a}{R_0}\right)^4 G_4\right] \quad (6)$$

For axial outside semi-elliptical surface cracks in cylinders, the tabular data of the influence coefficients G_0 and G_1 in API 579 [1] cover the t/R_i ratio in a range of 0 to 1, the a/t ratio in a range of 0 to 0.8, and the a/c ratio in a range of 0.03125 to 2. For axial surface cracks with a/c = 0 on the outside surface of cylinders, API 579 [1] covers the Ri/t ratio from 1 to 1000 and the a/t ratio from 0 to 0.8. In API 579, G_0 and G_1 are expressed in the following 6th-order polynomial functions of the parametric angle, and the coefficients were obtained by the curve fitting from the FEA results [9]:

$$G_0 = A_{00} + A_{10}\beta + A_{20}\beta^2 + A_{30}\beta^3 + A_{40}\beta^4 + A_{50}\beta^5 + A_{60}\beta^6 \quad (7)$$

$$G_1 = A_{01} + A_{11}\beta + A_{21}\beta^2 + A_{31}\beta^3 + A_{41}\beta^4 + A_{51}\beta^5 + A_{61}\beta^6 \quad (8)$$

where A_{ij} are the curve-fit parameters, their values are given in Table 9B.13 in API 579 [1]. Once G0 and G1 are obtained, the higher-order influence coefficients G2, G3 and G4 can be determined from G0 and G1 using the weight function approach, see Paragraph 9B.14.3 and 9B.14.4 in API 579 [1] for details.

2.4 Curve-fit solutions of the K factor

For simulating crack initiation or growth, the FFS analysis usually focuses on the K values at the deepest and surface points. The new surface crack profile is determined by crack increments. Recently, Xu et al. [11] obtained the best curve fit solutions of G1 and G2 in a closed-form format from the tabular data given in API 579 [1] at those two points for the API selected cylinder sizes. For ASME Section XI applications, crack depth does not exceed one half of the crack length, *i.e.*, $a/c \le 1$, and thus Xu et al. [11] utilized API tabular data within this limit on the crack aspect ratios in their curve fitting. For an arbitrary cylinder size or crack size, an interpolation is still needed to estimate the values of G0 and G1 at the two critical points.

3. DATA-DRIVEN SOLUTIONS OF THE K FACTOR BY MACHINE LEARNING

3.1 Machine learning and neural network

Recently, Zhu et al. [13] developed data-driven solutions of the K factors for axial outside surface cracks in cylinders in terms of the supervised machine learning technology, where ANN models were obtained through learning from previous experience (i.e., labeled input and output data) with built-in learning functions and algorithms. A brief technical review on the basic concepts, categories, architectures, activation functions, cost function, model error measures, and modeling procedures of the ANN approach was given by Zhu et al. [12].

An ANN model consists of three layers: input, hidden and output layers. The input layer is the first layer, and the output layer is the last layer. The layers between the input and output layers are named as "hidden layers" that contain hidden neurons. In general, the numbers of both hidden layers and hidden neurons are unknown and determined using the trial-and-error analysis. In many cases, one hidden layer is sufficient for engineering data analysis. In an ANN model, each neuron receives multiple input data, and then adds them through a simple analysis. After that, the combined results are processed with an activation function in a specific algorithm. The value processed with the activation function becomes an output value to other neurons in the next layer or a final output variable.

The connection between neurons of different layers is achieved by parametric weights that denote the strength of the connection. Signals received at neuron i can be described by a combined linear function:

$$u_i = \sum_{j=1}^{N} w_{ij} x_j + b_i \quad (9)$$

And the output data are processed by a transfer function:

$$y_i = f(u_i) \quad (10)$$

where u_i is the linear combined variable from the input data in Eq. (9); $x_1, x_2, \ldots, x_N$ are the independent input variables; N is the total number of input variables; y_i is the dependent output variable of the neuron that can be the final output or the input to another hidden layer; $w_{i1}, w_{i2}, \ldots, w_{iN}$ are the weights of input variables at neuron i; f is an activation function; and b_i is a bias.

An activation function is needed to introduce nonlinear real-world data to ANN models. This work adopts the commonly used sigmoid function, as shown in Fig. 1 to activate the connections of neurons between input and hidden layers, and a linear function is used to activate the connections of neurons between hidden and output layers.

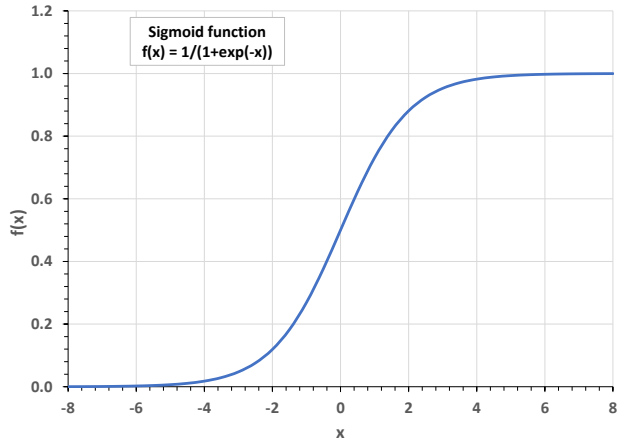

Figure 2. Sigmoid function

During the machine learning, an initial network architecture is created with assumed numbers of hidden layers and hidden neurons, and the ANN model is solved with assumed initial random values of weights and biases applied to the connections. Observation y_i enters the ANN model, and the output $\hat{y}_i$ is obtained. The model error between the ANN prediction $\hat{y}_i$ and the real observation y_i is measured in this analysis using the root mean squared error (RMSE):

$$RMSE = \sqrt{\frac{1}{N}\sum_{i=1}^{N}(y_i - \hat{y}_i)^2} \qquad (11)$$

3.2 Construction of ANN model

As discussed previously, API 579 [1] provides a series of FEA-based tabular data for the influence coefficients G0 and G1 of the K factor for axial outside surface cracks in cylinders with seven R_i/t ratios of 1, 3, 5, 10, 20, 60, and 100. In order to obtain an accurate data-driven model using ANN, this work only considers thin-walled cylinders with four R_i/t ratios of 10, 20, 60, 100 (i.e., D/t = 22, 42, 122, 202). For each cylinder, six crack aspect ratios are considered as a/c = 0.03125, 0.0625, 0.125, 0.25, 0.5, 1. For each crack aspect ratio, five crack depth ratios are considered as a/t = 0, 0.2, 0.4, 0.6, 0.8. This leads to a total of 4x6x5 = 120 data points for G0 (and G1) at the deepest (and surface) point for an axial outside surface crack in a thin-walled cylinder (D/t ≥ 20). These data points for G0 and G1 at the deepest and surface points are extracted from the data tables in API 579 and then used to train the ANN model.

The ANN functions of G0 and G1 are modeled separately in this work, and each of the two influence coefficients has three input variables: R_i/t, a/c, and a/t and one output variable: G0 or G1. On this basis, a three-layer ANN model is constructed, as illustrated in Fig. 3. In this model, the input layer has three input variables: X1 = R_i/t, X2 = a/c, and X3 = a/t, and the output layer has one output variable Y = G0 or G1. Based on our previous ANN models [3], it is assumed that this ANN model has one hidden layer with five hidden neurons. Thus, this ANN model denoting as 3x5x1 contains 20 weights and six biases. The training datasets extracted from API 579 are used for this ANN model to learn and to determine the 26 unknown parameters (weights and biases) through optimization via iterations. The Excel Solver is utilized to minimize the model error of RMSE, with the initial 26 unknown parameters to be taken as random values. Once a minimal RMSE error is reached, the model weights and biases are determined from the training datasets, and the ANN model is completely developed.

Note that the same ANN model shown in Fig. 3 is utilized to determine the data-driven models for both G0 and G1 at the deepest and surface points for axial outside semi-elliptical surface cracks in a thin-walled cylindrical pressure vessel, as discussed next.

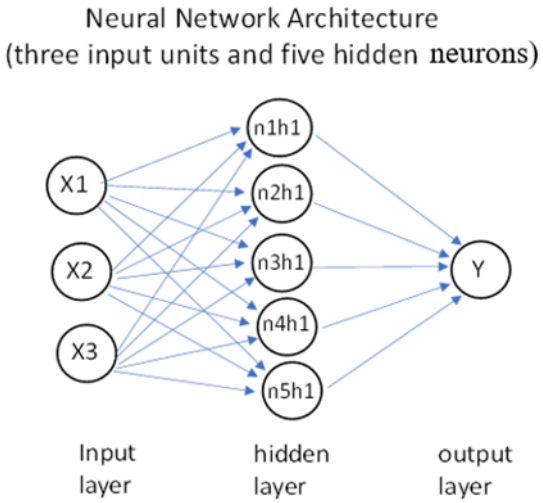

Figure 3. Architecture of a five-layer ANN model

3.3 Data-driven model of G0 at the deepest point

Figures 4(a) and 4(b) compare the ANN model predictions (i.e., output data) with the target data of G0 taken from API 579 at the deepest point of axial outside surface cracks for all training data points in normalized values and actual values, respectively. These figures show that the machine learning predictions from the ANN model agree very well with the target data of G0 taken from API 579 at the deepest point, and the goodness-of-fit measure is obtained as R^2 = 0.9976 for all training data points. This indicates that the proposed ANN model is very accurate for predicting the G0 values at the deepest point for the axial outside surface cracks in thin-walled cylinders (D/t ≥ 20) compared to the tabular data of G0 given in API 579.

Figures 5(a) to 5(c) compares the ANN model predictions with API data of G0 at the deepest point for three API selected thin-walled cylinders of R_i/t = 10, 20, and 60. Again, it is observed from these three figures that the ANN model predictions match closely with the API data of G0 at the deepest point of the surface crack for the API selected thin-walled cylinders. Further inspection shows that the ANN model errors for most data points are less than 2%. Due to the space limitation, the similar trends and results of G0 are obtained for the thinnest-walled cylinder with R_i/t = 100, but not shown here.

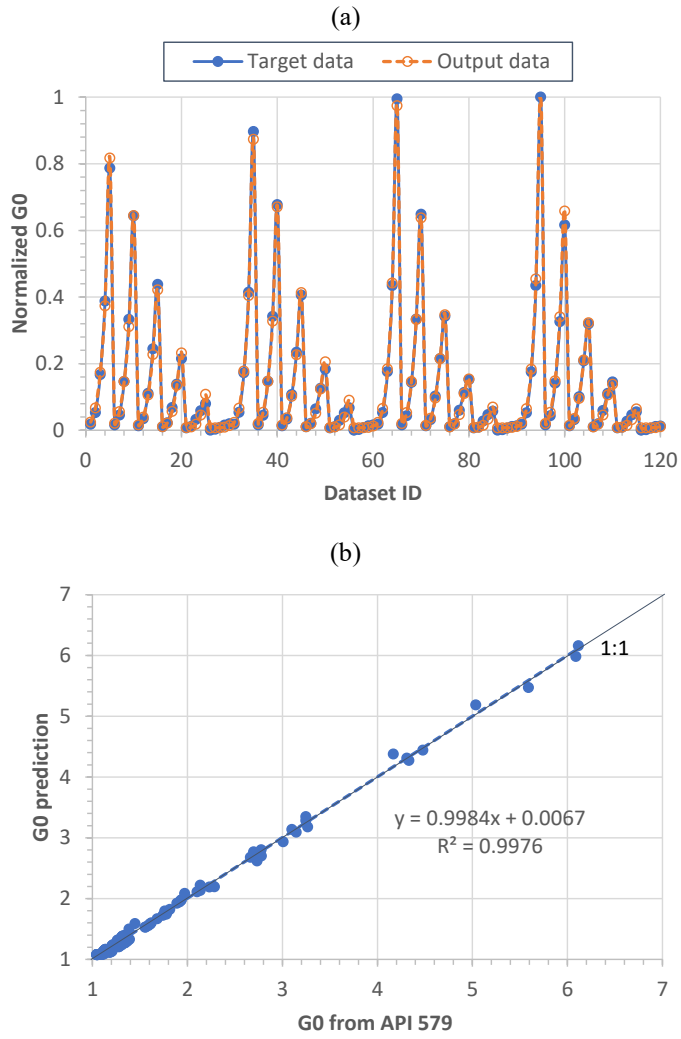

Figure 4. Comparison of ANN model predictions with target data of G0 at the deepest point from API 579 (a) normalized values, and (b) actual values

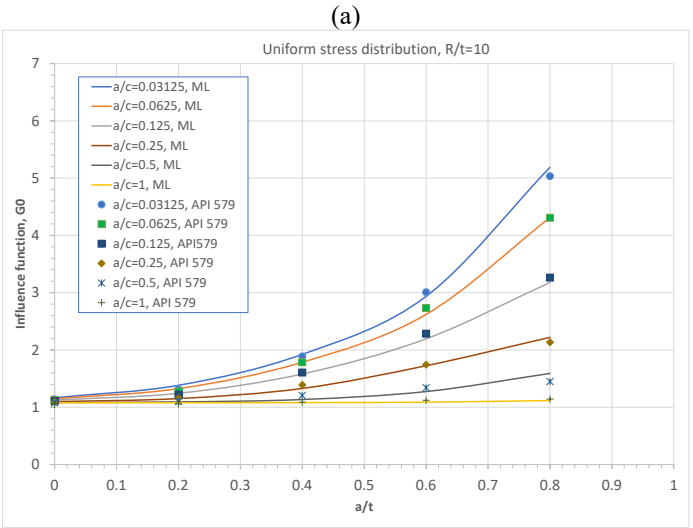

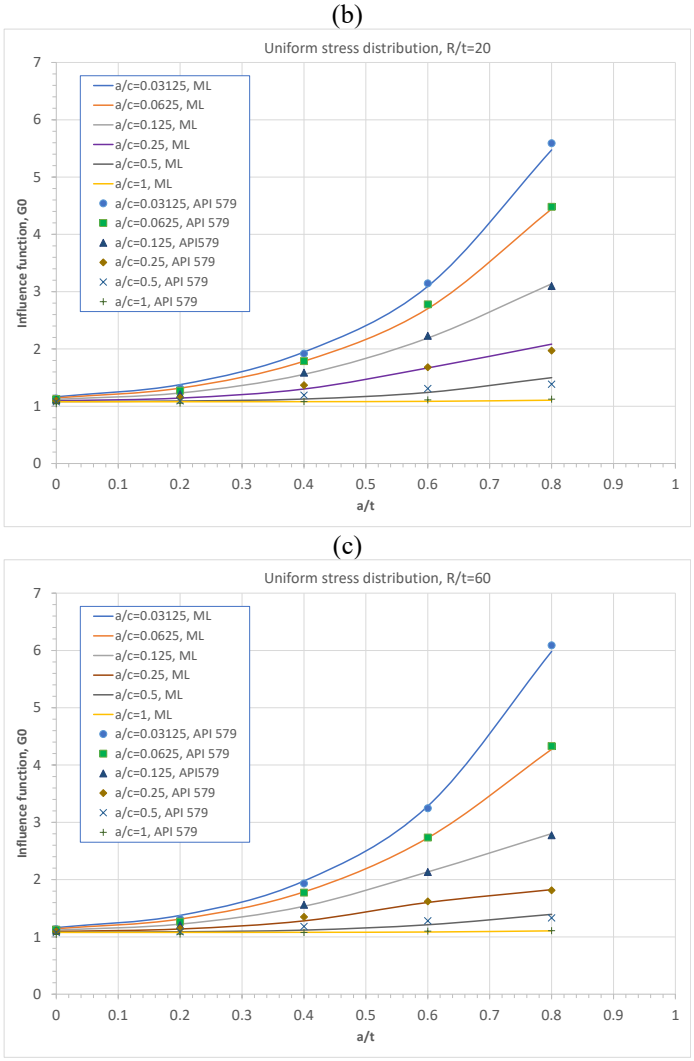

Figure 5. Comparison of ANN predictions with API data of G0 at the deepest point for (a) $R_i/t=10$, (b) $R_i/t=20$, (c) $R_i/t=60$

3.4 Data-driven model of G1 at the deepest point

Figures 6(a) and 6(b) compare the ANN model predictions (output data) with the target data of G1 taken from API 579 at the deepest point of axial outside surface cracks for all training data points in normalized values and actual values, respectively. These figures show that the ANN model predictions agree closely with the target data given by API 579 at the deepest point, and the goodness-of-fit measure is obtained as $R^2 = 0.9913$ for all training data points. This indicates that the proposed ANN model is very accurate for predicting the G1 value at the deepest point in comparison to the tabular data of G1 given in API 579.

Figures 7(a) to 7(c) compare the ANN model predictions with API data of G1 at the deepest point for three API selected cylinder sizes of R_i/t = 10, 20, and 60. Again, it follows from these three figures that the ANN model predictions match well with the API data of G1 for all thin-walled cylinders considered in API 579, and further inspection shows that the ANN model errors at most data points are less than 2%.

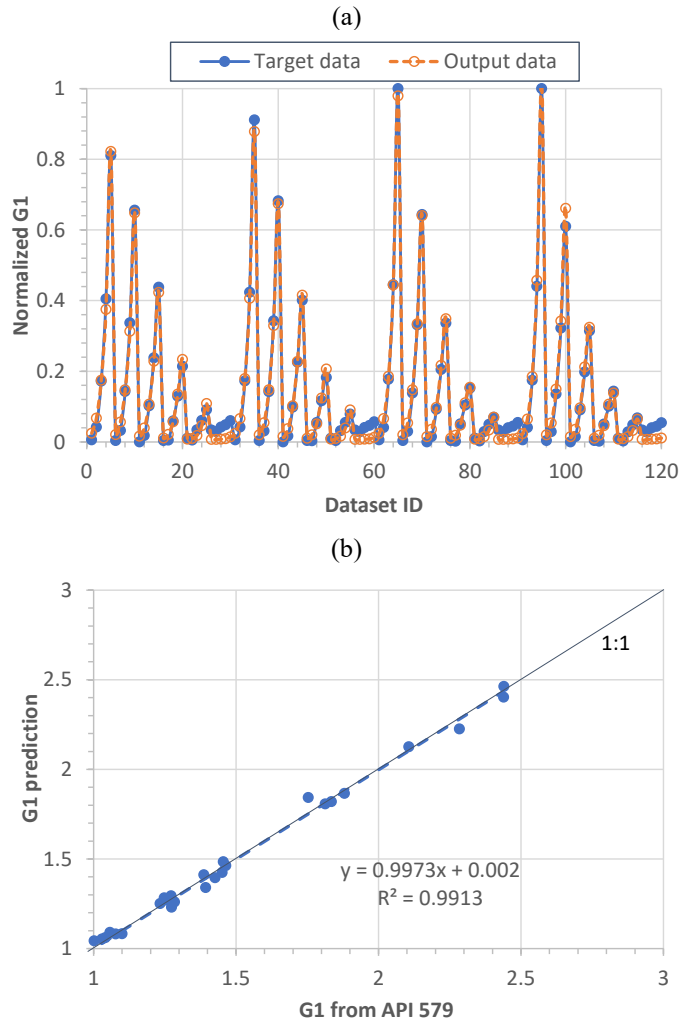

Figure 6. Comparison of ANN model predictions with target data of G1 at the deepest point from API 579 (a) normalized values, and (b) actual values

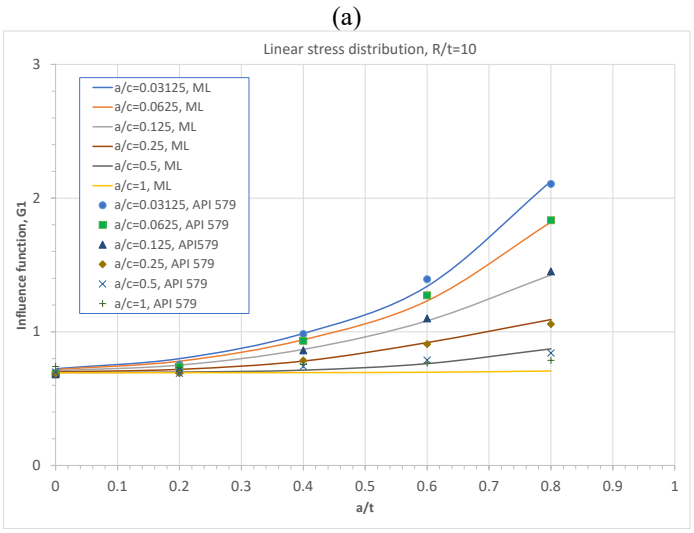

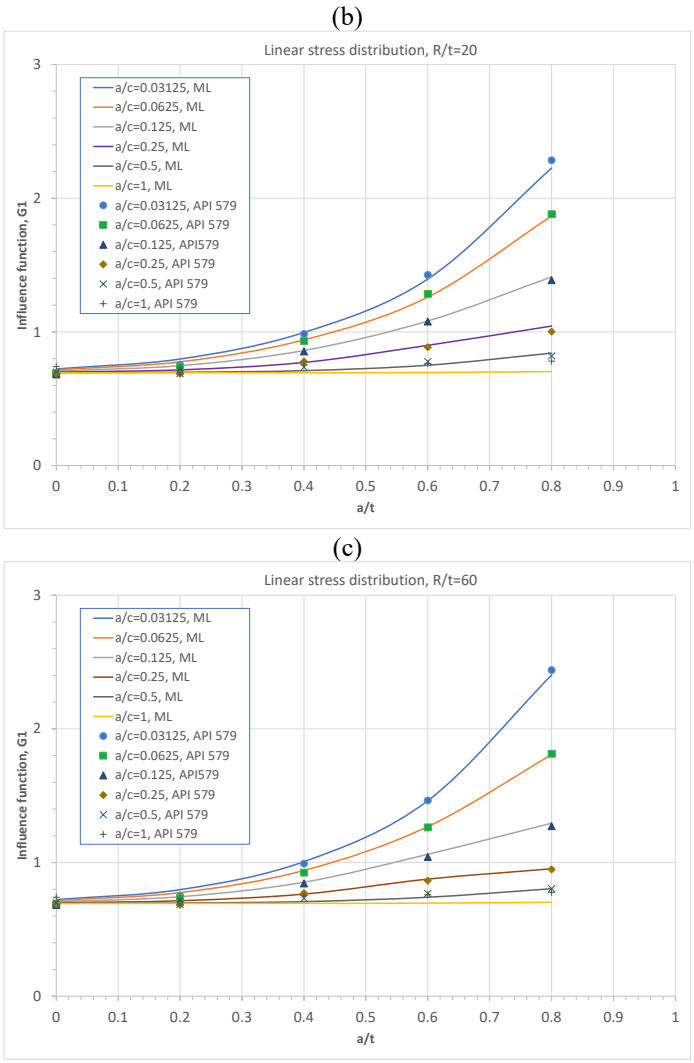

Figure 7. Comparison of ANN predictions with API data of G1 at the deepest point for (a) R_i/t=10, (b) R_i/t=20, (c) R_i/t=60

3.5 Data-driven model of G0 at the surface point

Figures 8(a) and 8(b) compare the ANN model predictions (output data) with the target data of G0 taken from API 579 at the surface point of axial outside surface cracks for all training data points in normalized values and actual values, respectively. These figures show that the ANN model predictions agree with most of API target data at the surface point, and the goodness-of-fit measure is obtained as $R^2 = 0.9986$ for all training data points. This indicates that the proposed ANN model is accurate for predicting the G0 value at the surface point in comparison to the tabular data of G0 given in API 579.

Figures 9(a) to 9(c) compare the ANN model predictions with API data of G0 at the surface point for three API selected cylinder sizes of R_i/t = 10, 20, and 60. Again, it is observed from these figures that the ANN model predictions match well with the API data of G0 for all thin-walled cylinders considered in API 579, and further inspection shows that the ANN model errors at most data points are less than 5%.

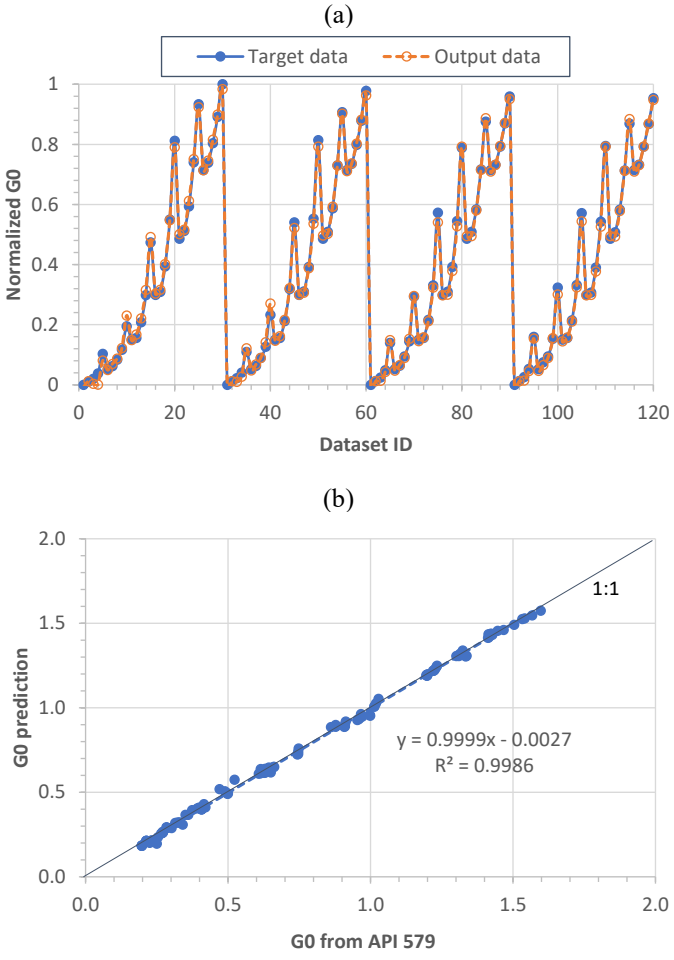

Figure 8. Comparison of ANN model predictions with target data of G0 at the surface point from API 579 (a) normalized values, and (b) actual values

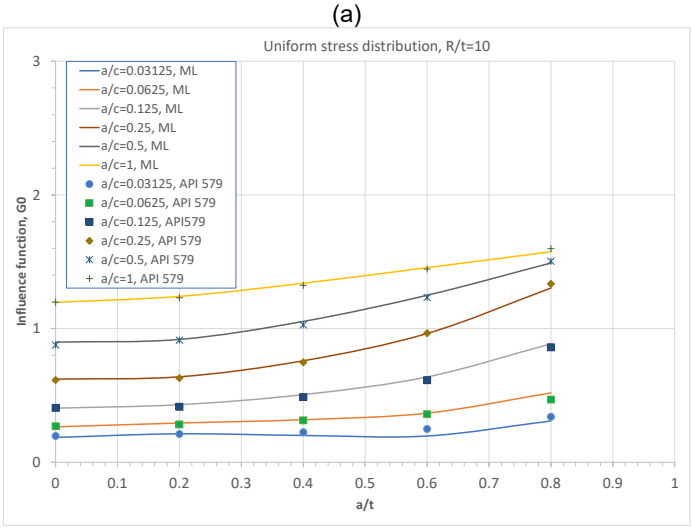

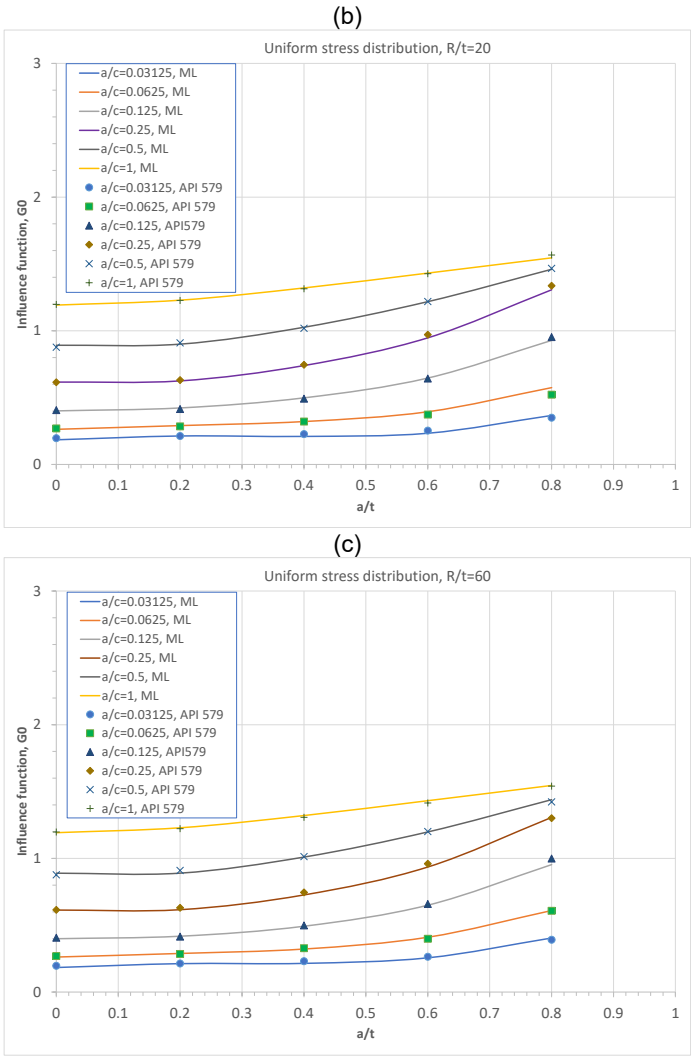

Figure 9. Comparison of ANN predictions with API data of G0 at the surface point for (a) $R_i/t=10$, (b) $R_i/t=20$, (c) $R_i/t=60$

3.6 Data-driven model of G1 at the surface point

Figures 10(a) and 10(b) compare the ANN model predictions (output data) with the target data of G1 taken from API 579 at the surface point of axial outside surface cracks for all training data points in normalized values and actual values, respectively. It is shown that the ANN model predictions agree with most of API given data at the deepest point, and the goodness-of-fit measure is obtained as $R^2 = 0.9925$ for all training data points. This indicates that the proposed ANN model is accurate for predicting the G1 value at the surface point in comparison to the tabular data of G1 given in API 579.

Figures 11(a) to 11(c) compare the ANN model predictions with API data of G1 at the surface point for three API selected cylinder sizes of $R_i/t = 10$, 20, and 60. Again, it is observed from these figures that the ANN model predictions match well with the API data of G1 for the cylinders considered in API 579, and further inspection shows that the ANN model errors at most points are less 5%.

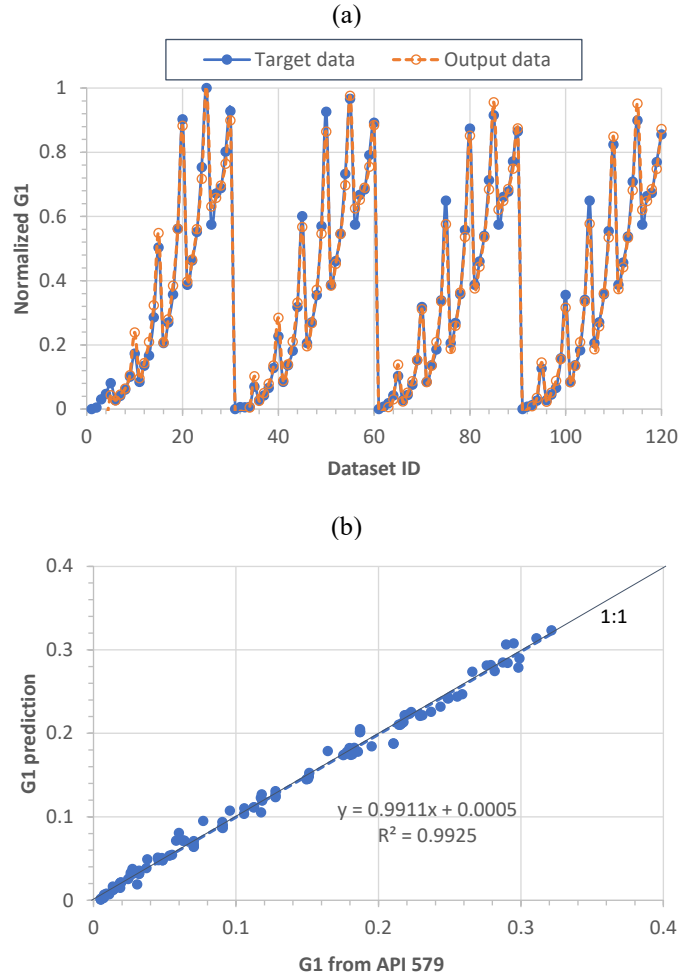

Figure 10. Comparison of ANN model predictions with target data of G1 at the surface point from API 579 (a) normalized values, and (b) actual values

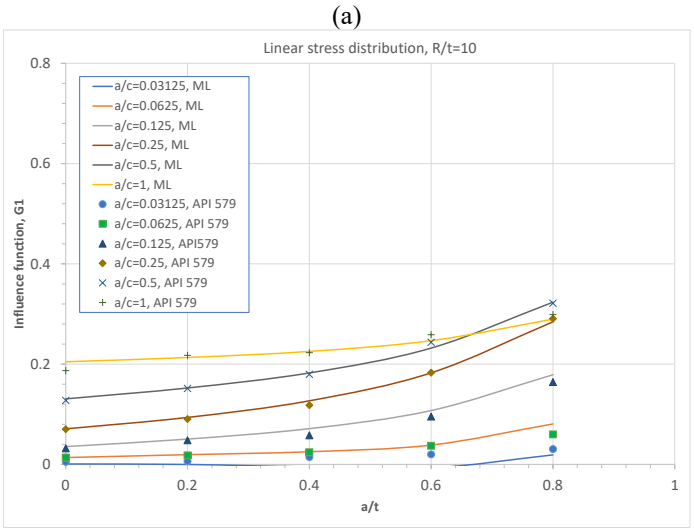

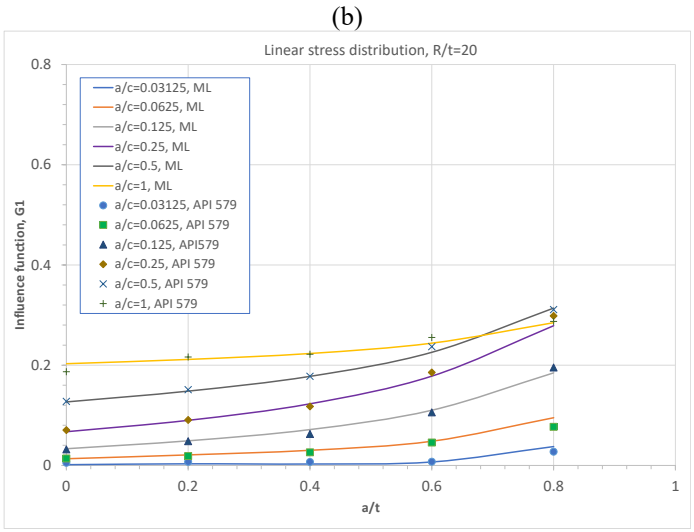

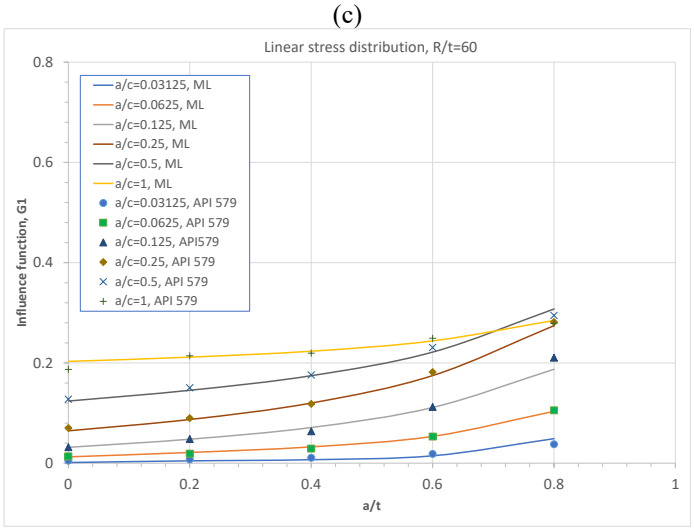

Figure 11. Comparison of ANN predictions with API data of G1 at the surface point for (a) R_i/t=10, (b) R_i/t=20, (c) R_i/t=60

4. Validation of ANN models

4.1 Validation by the curve-fit solutions

The ANN models of G0 and G1 developed above are evaluated using the curve-fit solutions obtained by Xu et al. [11]. Figures 12 and 13 compare the ANN model predictions of G0 and G1 with the curve-fit solutions obtained by Xu et al. [11] for axial outside semi-elliptical surface cracks at the deepest point for R_i/t = 10 (i.e., D/t = 22). These figures show that the ANN model predictions agree well with the curve-ft results for different crack lengths and crack depths under consideration. Similar good agreements between the ANN models and curve-fit solutions of G0 and G1 are also observed for other thin-walled cylinders (R_i/t = 20, 60, and 100) at the deepest and surface points. These observations indicate that the ANN models of G0 and G1 have the similar accuracy to the curve-fit solutions.

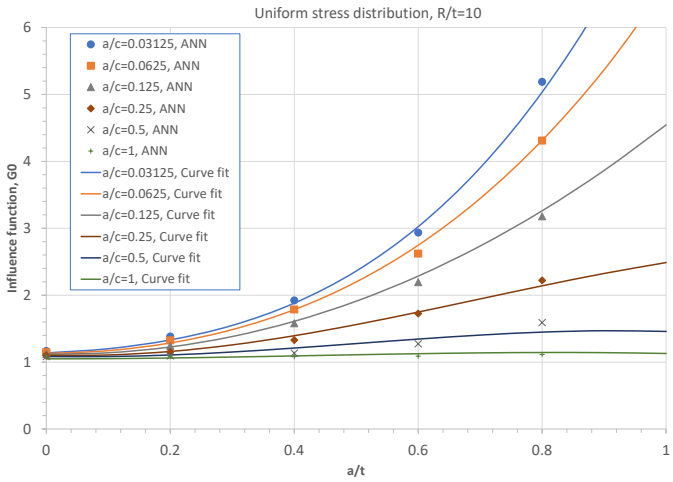

Figure 12: Comparison of ANN model predictions with the curve-fit solutions of G0 at the deepest point for $R_i/t = 10$

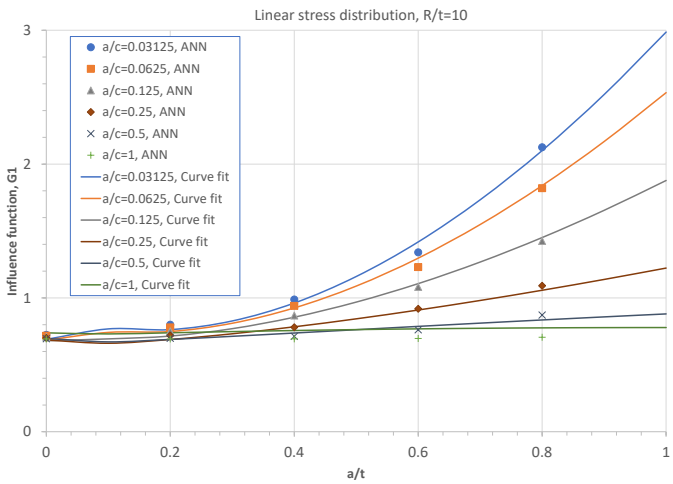

Figure 13: Comparison of ANN model predictions with the curve-fit solutions of G1 at the deepest point for $R_i/t = 10$

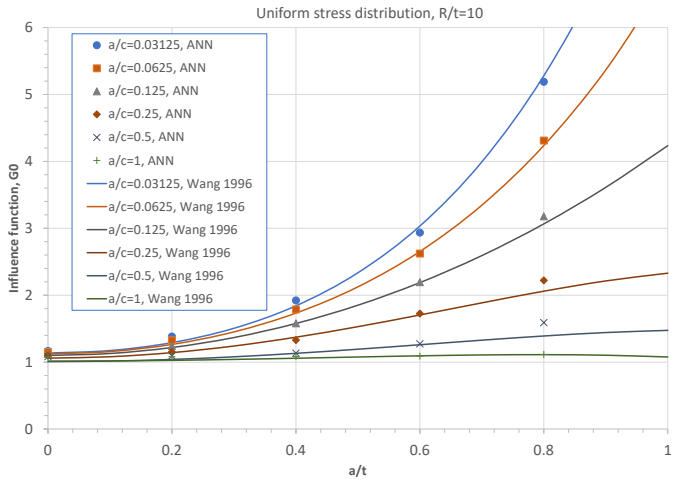

Figure 14: Comparison of ANN model predictions with the weight function solutions of G0 at deepest point for $R_i/t = 10$

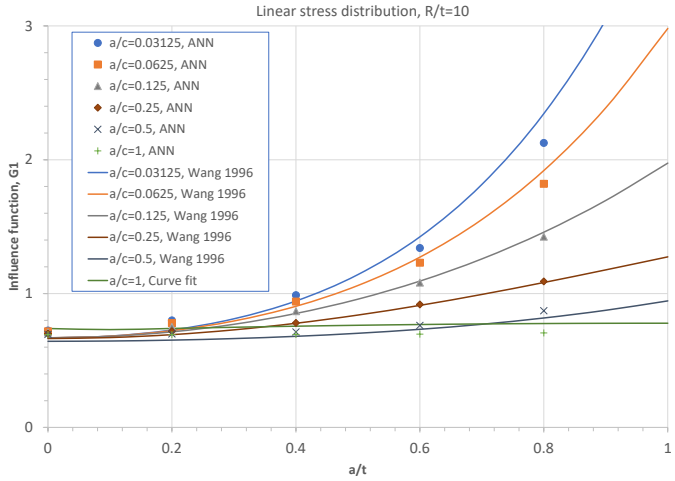

Figure 15: Comparison of ANN model predictions with the weight function solutions of G1 at deepest point for $R_i/t=10$

4.2 Validation by the weight function solutions

Based on the FEA results and the weight function method, Wang and Lamber [8] in 1996 developed a closed-form solution of the K factor for a thin-walled pipe with $R_i/t = 10$. Figures 14 and 15 compare the ANN model predictions of G0 and G1 with the closed-from solutions obtained by Wang and Lamber [8] for axial outside semi-elliptical surface cracks at the deepest point for $R_i/t = 10$. These figures show that the ANN model predictions agree closely with the curve-ft results for different crack lengths and crack depths under consideration. These observations show that the ANN models of G0 and G1 have the similar accuracy to the the curve-fit solutions or the weight function solutions, and thus the proposed ANN models of G0 and G1 are validated by the curve-fit solutions and the weight function solutions for the axial outside surface cracks in thin-walled cylinders.

5. CONCLUSIONS

This paper briefly reviewed the estimate method of stress intensity factor given in API 579 for axial semi-elliptical surface cracks in pressurized cylinders and the curve-fit solutions of the influence coefficients G0 and G1 of the stress intensity factor that were obtained by Xu et al. [11] at the deepest and surface points. The curve-fit solutions of G0 and G1 are only applicable to the API selected cylinder sizes. For other cylinders, complex interpolations are needed based on the R_i/t ratios. To avoid this, the present paper adopted ANN and developed four data-driven models of G0 and G1 for axial outside surface cracks at the deepest and surface points. The model predictions of G0 and G1 is a general function of cylinder size (t/R_i), aspect ratio (a/c), and crack depth (a/t). From the results, the following conclusions are drawn:

(1) The ANN modeling is an efficient machine learning approach used to determine data-driven models of stress intensity factors for the complex 3D surface problems.
(2) The proposed ANN models are adequate to use for predicting accurate values of the influence coefficients G0 and G1 for axial outside surface cracks in thin-walled cylinders at the deepest and surface points.
(3) The proposed ANN models of G0 and G1 for axial outside surface cracks in thin-walled cylinders are accurate, and have been validated by the existing curve-fit solutions and the weight function solutions.
(4) With the predicted values of G0 and G1, the stress intensity factor solution can be estimated for an axial outside surface crack in a thin-walled cylinder, and then the crack initiation or growth analysis can be performed for the thin-walled cylinder in an FFS evaluation.

ACKNOWLEDGEMENTS

This work was partially supported by the Laboratory Directed Research and Development (LDRD) program within the Savannah River National Laboratory (SRNL). This document was prepared in conjunction with work accomplished under Contract No. 89303321CEM000080 with the U.S. Department of Energy (DOE) Office of Environmental Management (EM).

REFERENCES

[1] API 579-1/ASME FFS-1, *Fitness-for-Service*, API Publishing Service, June 2016.
[2] ASME Boiler and Pressure Vessel Code (BPVC), 2021 Edition, *Rules for Inservice Inspection of Nuclear Power Plant Components*, Section XI, Division 1, Appendix A.
[3] Underwood J H. "Stress Intensity Factors for Internally Pressurized Thick-Walled Cylinders," *Stress Analysis and Growth of Cracks, ASTM STP 513*, American Society for Testing and Materials, 1972, pp. 59-70.
[4] Kobayashi A S. "A Simple Procedure for Estimating Stress Intensity Factors in Regions of High Stress Gradient," *Significance of Defects in Welded Structures*, University of Tokyo Press, 1974, pp. 127-143.
[5] Kobayashi AS, Polvanich N, Emery AF, Love WJ. "Inner and Outer Surface Cracks in Internally Pressurized Cylinders," *Journal of Pressure Vessel Technology*, Vol. 99, 1977: 83-89.
[6] Newman JC, Raju IS. "Stress-Intensity Factors for Internal Surface Cracks in Cylindrical Pressure Vessels," *Journal of Pressure Vessel Technology*, Vol. 102, 1980: 342-346.
[7] Raju IS, Newman JC. "Stress-Intensity Factors for Internal and External Surface Cracks in Cylindrical Vessels," *Journal of Pressure Vessel Technology*, Vol. 104, 1982: 293-298.
[8] Wang X, Lambert SB. "Stress Intensity Factors and Weight Functions for Longitudinal Semi-Elliptical Surface Cracks in Thin Pipes," *International Journal of Pressure Vessels and Piping*, Vol. 65, 1996: 75-87.
[9] Anderson TL, Thorwald G, Revelle DJ, Osage DA, Janelle JL, Fuhry ME. "Development of Stress Intensity Factor Solutions for Surface and Embedded Cracks in API 579," *WRC Bulletin 471*, Welding Research Council, May 2002.
[10] Xu SX, Lee DR, Scarth DA, Cipolla RC. "Closed-form Relations for Stress Intensity Factor Influence Coefficients for Axial ID Surface Flaws in Cylinders for Appendix A of ASME Section XI," *Proceedings of ASME Pressure Vessels and Piping Conference*, July 20-24, 2014, Anaheim, CA, USA. PVP2014-28222.
[11] Xu SX, Lee DR, Scarth DA, Cipolla RC. "Closed-form Relations for Stress Intensity Factor Influence Coefficients for Axial Outside Surface Flaws in Cylinders for Appendix A of ASME Section XI," *Proceedings of ASME Pressure Vessels and Piping Conference*, July 17-21, 2016, Anaheim, CA, USA. PVP2016-64023.
[12] Zhu XK, Johnson WR, Sindelar R, Wiersma B. Artificial neural network models of burst strength for thin-wall pipelines, *Journal of Pipeline Science and Engineering*, Vol. 2, 2022: 100090.
[13] Zhu XK, Zhu JB, A Duncan, Data-driven stress intensity factor solutions for axial outside surface cracks in thick-wall cylinders, *Proceedings of the ASME Pressure Vessels & Piping Conference*, July 17-22, 2022, Las Vegas, Nevada, USA.
[14] Timoshenko S. *Strength of Materials – Advanced Theory and Problems*, D Van Nostrand Company, New York, 1956.